

# Nano-Domain Pinning in Ferroelastic-Ferroelectrics by Extended Structural Defects

Yachin Ivry,\* Colm Durkan, Daping Chu, and James F. Scott\*

Most ferroelectrics are also ferroelastics (hysteretic stress-strain relationship and response to mechanical stresses). The interactions between ferroelastic twin walls and ferroelectric domain walls are complex and only partly understood, hindering the technological potential of these materials. Here we study via atomic force microscopy the pinning of 180-degree ferroelectric domain walls in lead zirconate titanate (PZT). Our observations satisfy all three categories of ferroelectric-ferroelastic domain interaction proposed by Bornarel, Lajzerowicz, and Legrand.

## 1. Introduction

In most ferroelectric crystals the crystal class changes at the Curie temperature,  $T_c$ , so that the systems are necessarily also ferroelastic.<sup>[1]</sup> Namely, there is a hysteresis in the stress-strain relationship and the domains respond to mechanical stresses<sup>[2–5]</sup> or more generally, there is a coexistence of patterns that can move under mechanical stress and patterns that respond to electric excitations.<sup>[6]</sup> However, the ferroelastic domain walls (usually termed “twin boundaries”) are generally not coincident with the macroscopic and mesoscopic ferroelectric polarization domain walls. For instance, ferroelastic domain walls can arise prior to ferroelectric domains,<sup>[7]</sup> while in thin films, a domain with a uniform out-of-plane polarization can span several twinning domains. The interaction between

elastic twins and polarization domain walls is complicated,<sup>[8–10]</sup> especially in multiferroics with magnetic domains in addition.<sup>[11]</sup> Two geometric hierarchies arise that are of significant interest: (1) ferroelastic nano-twins that lie inside ferroelectric meso-domains, as first shown by Simon *et al.*<sup>[12]</sup> and more recently by Evans *et al.*<sup>[11]</sup> and (2) the converse situation with ferroelectric nano-domains inside ferroelastic twins.<sup>[13]</sup> These situations produce curious effects, including self-similar domain geometries<sup>[14]</sup> and acute sensitivity to irradiation from electron microscopes,<sup>[15,16]</sup> and unintentional stress.<sup>[17]</sup>

As ferroelectric thin films are a topic of great current interest, much has been discovered about the interaction of ferroelectric domain walls with oxygen vacancy gradients near electrode interfaces and with misfit deformations that arise from the difference in lattice constants between substrate and film (dislocations have also been reported<sup>[18]</sup>). Much less is known about the role of other extended structural defects, however. In the present paper, we show the role of extended defects in pinning and distorting ferroelectric domain walls in PZT on an atomic scale. The depinning of similar sites has been studied previously by Tybell, Paruch and Triscone<sup>[19]</sup> and modelled with a creep theory, giving creep exponents.<sup>[19–22]</sup>

There are additional lattice defects of importance in our data. These include discontinuous slips or steps in the ferroelastic twin planes and thin layers of in-plane domains sandwiched between larger out-of-plane domains.

We found that our results are consistent with the theoretical framework developed by Bornarel *et al.*<sup>[2]</sup> and we propose a quantitative method to evaluate the energy associated with pinning.

## 2. Experimental Procedure

We examined thin films of the commonly used ferroelectric material PZT due to its relatively high piezoresponse. This high electro-mechanical coupling has utilized PZT in technologies ranging from medical imaging systems to cellular communication devices. In addition, the strong piezoresponse aids experimental investigations. The material under examination was a  $t = 60$  nm thick  $\text{PbZr}_{0.3}\text{Ti}_{0.7}\text{O}_3$  film, far from the morphotropic phase boundary as described elsewhere.<sup>[23]</sup> We chose to study a polycrystalline material, where in first approximation, large individual grains can be considered as isolated crystallites, expediting the research. To study

Dr. Y. Ivry  
Research Laboratory of Electronics  
Massachusetts Institute of Technology  
77 Massachusetts Avenue  
Cambridge, Massachusetts 02139, USA  
E-mail: ivry@mit.edu

Dr. Y. Ivry, Dr. C. Durkan  
Nanoscience Centre  
University of Cambridge  
11 JJ Thomson Avenue  
Cambridge CB3 0FF, UK

Prof. D. Chu  
Electrical Engineering Division  
University of Cambridge  
9 JJ Thomson Avenue  
Cambridge CB3 0FA, UK

Prof. J. F. Scott  
Department of Physics  
Cavendish Laboratory  
University of Cambridge  
Madingley Road, Cambridge CB3 0HE, UK  
E-mail: jfs32@cam.ac.uk



DOI: 10.1002/adfm.201304268

the simultaneous ferroelectric-ferroelastic domain distribution we used piezoresponse force microscopy (PFM)<sup>[22,23]</sup> in its enhanced-mode (E-PFM).<sup>[24,25]</sup> Similarly to conventional PFM, in E-PFM, the signal corresponds to a mechanically oscillating tip that is in-contact with a ferroelectric film. These oscillations are due to the inverse piezoelectric effect in the ferroelectric film, upon which an AC field is applied. E-PFM allows enhanced imaging performances (higher resolution and sensitivity)<sup>[26]</sup> by extending the three main limitations of the conventional PFM framework: (1) the AC frequency is driven close to (~95%) the first in-contact resonance; (2) the AC amplitude is comparable to, or exceeds the DC coercive value of the film; and (3) soft (*e.g.*, 0.2 N/m) cantilevers are used. In comparison, the conventional PFM framework requires that the driving frequency and amplitude will be kept around an order of magnitude lower than the first in-contact resonance and the DC coercive value, respectively, while stiff ( $\geq 10$  N/m) cantilevers are required. In addition to the high-imaging performances, the two imaging modes of E-PFM allow a clear distinction between the different domain types. Specifically, *amplitude* imaging is sensitive mainly to ferroelastic (twinning) domains. Ferroelectric domain walls that exhibit no out-of-plane polarization are also observable, but not the ferroelectric (up and down out-of-plane polarization) domains themselves. Likewise, ferroelectric domains, *i.e.*, areas with a well-defined component of out-of-plane polarization, are observed with *phase* mode imaging. Finally, the topography of the explored area is also simultaneously mapped with standard atomic force microscopy (AFM) imaging. As a matter of convenience we used in this paper a color scheme of orange, grey, and blue for the amplitude, phase and topography images, respectively (for the schematically-drawn domains, we used orange for out-of-plane crystallographic domains that contribute to the ferroelectric polarization, and blue for the in-plane ferroelastic domains).

### 3. Results: Static Pinned Domain

In a polycrystalline material, grains that are much larger than the film thickness can generally be treated as an individual crystallite. **Figure 1** shows the domain distribution in such a grain. There are two distinguishable regions with periodic ferroelastic twinned stripe domains (separated with a blue dashed line); in each of these regions all stripes are pointing towards the same direction as was revealed with the amplitude image (Figure 1a). Such groups of periodic ferroelastic striped domains that share a common orientation are called bundle domains and have

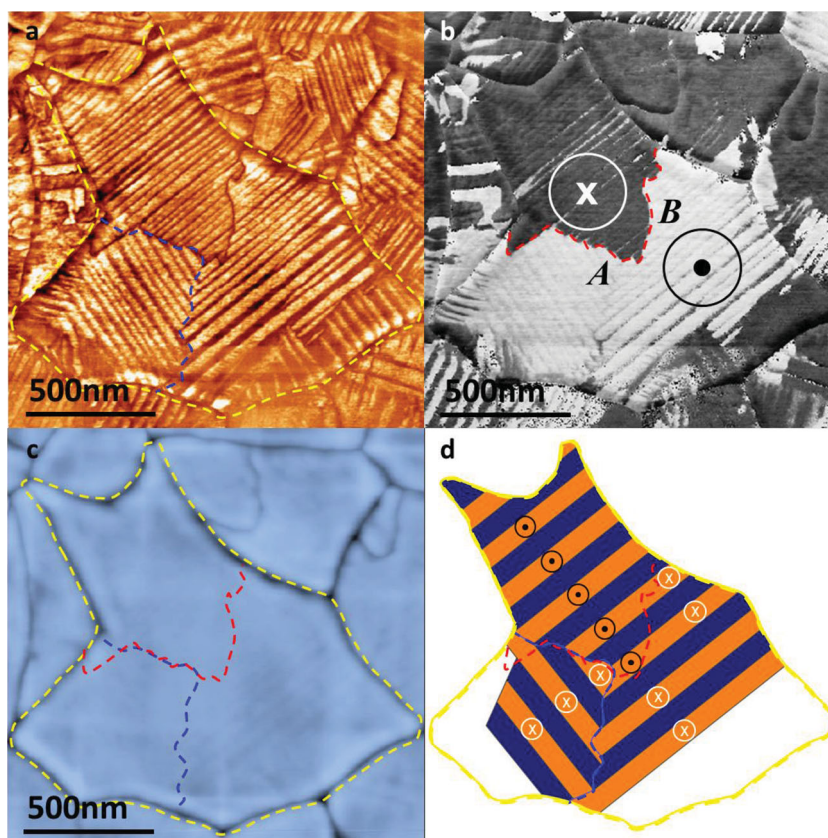


**Figure 1.** Mesoscopic ferroelectric and ferroelastic domain distribution in a PZT crystallite observed with E-PFM. (a) The ferroelastic domains in the large grain form two main regions with periodically alternating (out-of-plane and in-plane) striped crystallographic domains, *i.e.*, bundle domains, or a mesoscopic ferroelastic domain. The bundle domain boundary is highlighted with a dashed blue line. (b) The mesoscopic out-of-plane polarization (the out-of-plane polarization of the *c* domains within a bundle domain) of the same area is also divided to two main mesoscopic ferroelectric domains, polarized up and down. The mesoscopic ferroelectric domain wall is highlighted by a dashed red line. (c) The simultaneously imaged topography in which some of the ferroelastic striped domains are apparent is given as a reference. (d) Schematic illustration of the *a* and *c* ferroelastic (blue and orange stripes) and ferroelectric (designated by arrows) domain distribution in the crystallite.

recently been characterized as meta-elastic domains which are higher level of hierarchy (longer characteristic length scale) than standard ferroelastic domains.<sup>[9,27]</sup> Likewise, the phase image (Figure 1b) demonstrates that there are two main mesoscopic out-of-plane polarization (ferroelectric) domains in this grain. These domains are designated by in and out arrows in Figure 1b (these ferroelectric domains are considered as *mesoscopic* domains because they include both stripes with in-plane and with out-of-plane polarization). The dashed red line in Figure 1c highlights the ferroelectric domain boundary between the two main bundle domains. It should be noted that the appearance of the striped domains also in the topography image (Figure 1c) confirms that these are indeed periodically alternating *a* and *c* ferroelastic domains, *i.e.*, areas in which all of the tetragonal unit cells align their long axis in- and out- of-plane, respectively. In addition, the zero signal of the in-plane ferroelastic domains in the piezoresponse phase image also confirms the ferroelastic domain distribution. The schematics in Figure 1d help illustrate the domain distribution in the grain.

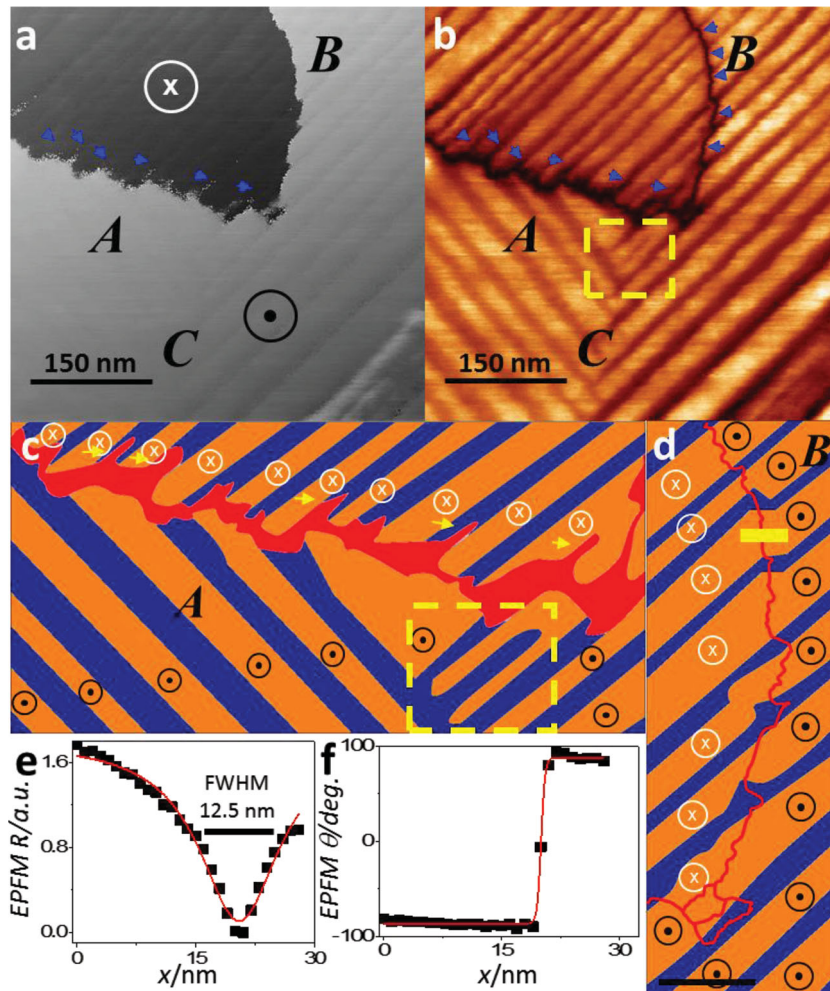


**Figure 2.** Nanoscopic crystallographic and ferroelectric domain distribution around pinned mesoscopic ferroelastic and polarization domain walls. 512 × 512 nm<sup>2</sup> E-PFM images of (a) the out-of-plane polarization (phase mode) and (b) the ferroelastic domain (amplitude mode) distribution around the mesoscopic ferroelectric and bundle domains of the crystallite from Figure 1. (c) Detailed schematic illustration of the domain distribution at an area (345 × 170 nm<sup>2</sup>) around the shared mesoscopic ferroelectric-ferroelastic domain wall at boundary A. The depolarization area (red) is disordered and has sharp bursts around at the  $a_1$ - $c$ - $a_2$  intersections (highlighted with yellow arrows). A split ferroelastic domain is highlighted with the dashed yellow rectangle. (d) Detailed schematics of the domain distribution in an area (100 × 297 nm<sup>2</sup>) around wall B demonstrates local distortion of the ferroelastic striped domains close to the ferroelectric domain wall (enlargement of the E-PFM micrographs from the areas presented in (c-d) are given in Figure S11). (e) Amplitude and (f) phase signals of 29 averaged sequential cross-sections that go through the ferroelectric domain wall (the area is highlighted with a yellow line in (d)). Red lines in (e) and (f) are the best fits to a Lorentzian and hyperbolic tangent functions, respectively, indicating a 12.5 nm domain-wall full width half maximum width (FWHM) and 0.5 nm (comparable with the pixel resolution) jump in the phase signal ( $\Delta x$ ).

Since we are interested in exploring the interplay between ferroelectric domain walls and extended structural defects in the material, we scanned a smaller area (512 × 512 nm<sup>2</sup>) around the boundary between the two opposite ferroelectric domains (Figure 2). We distinguish between two parts of the domain wall, denoted by A and B in Figures 1 and 2: (A) a mesoscopic ferroelectric polarization domain wall that coincides with a bundle domain boundary. Here, the ferroelectric domain wall coincides with the place where the orientation of

the striped ferroelastic domains is changed. This domain wall is the meeting point for  $a_1$ ,  $a_2$  and  $c$  stripes, and hence is accompanied by multiple twinning defects. The second part of the mesoscopic ferroelectric domain wall (B) is a 180° ferroelectric domain wall in the middle of striped ferroelastic domains (... $a/c/a/c...$ ) within a bundle domain. This ferroelectric domain wall is perpendicular to the continuous ... $a/c/a/c...$  stripes. Therefore, as opposed to domain wall A, domain wall B is presumably not accompanied by a collective abrupt change of the twinning plane direction. An additional domain wall (C) represents an intersection between two bundle domains (*i.e.*, ... $a_1/c/a_2/c/a_1/c/a_2...$  wall) while the out-of-plane polarization in the two neighboring bundle domains is similar *i.e.*, the domain wall is of the form: ... $a_1/c^+/a_2/c^+/a_1/c^+/a_2...$ , as can be seen in Figure 2.

We are interested in examining the influence of extended structural defects on ferroelectric domain walls. Hence, we are concerned mainly with domain walls A and B. To facilitate a better examination of these two domain wall areas (A and B), we sketched the nanoscale crystallographic (ferroelastic) and out-of-plane polarization (ferroelectric) domain distributions around walls A (Figure 2c) and B (Figure 2d). This allowed us to examine the extended structural defects and domain wall properties associated with each of these two areas.

The multiple twinning walls that exist in the bundle domain wall at A correspond to a high concentration of crystallographic defects. That is, in addition to the periodic  $a$ - $c$  twinning walls (*i.e.*, plane defects) that are found in any bundle domain, each  $a$ - $c$  domain intersection is accompanied by an  $a_1$ - $a_2$  twinning plane defect, increasing the dimensionality of the crystallographic defects and hence also the effective ferroelectric domain wall size. Finally, Figure 2c shows that another deformation of the crystal takes place in the striped domains, as they become sharp bursts and wedge-shaped (Figure 2b-c), unlike, for instance, the unperturbed bundle boundary in wall C.

As opposed to boundaries A and C, which act as ferroelastic domains walls, Boundary B (Figures 2a-b) separates only between up and down polarization domains that are within the same continuous striped domains. Thus, presumably, the crystallographic structure around boundary B is unperturbed. However, a careful look at Figure 2d reveals that the crystallographic structure around boundary B is defected. Here, the defects occur when the stripe is distorted close to the ferroelectric domain wall. These defects are highlighted by arrows in

Figure 2b and clearly observable in Figure 2d (enlargement of the E-PFM images from the areas presented in (c-d) are given in Figure S11). This distortion introduces local changes in the twinning plane direction and effectively adds more twinning planes in the area, which act as local zigzag twinning walls, similar to the case of a bundle domain boundary; but with fewer intersections of the twinning planes. We would also like to draw the reader's attention to the fact that all the distorted ferroelastic stripes are indented towards the same direction, giving rise to an effective correlation. However, this correlation is not as strong as in the case of a bundle domain boundary.

We also wished to characterize the mesoscopic ferroelectric domain walls. Since the ferroelectric domain walls are depolarized, these walls stand out clearly in the amplitude image (Figure 2b), allowing an immediate comparison between the domain wall thickness and structure of these two depolarization regions (also appear in Figures 2c-d, where they are designated in red). Specifically, two main differences are clearly noticed in the two depolarization areas. First, while the transition between the two opposite out-of-plane polarization (ferroelectric) domains in *B* is abrupt and sharp, the depolarization area (ferroelectric domain wall) of domain boundary *A* is of a much more disordered nature. In particular, in some areas, near the  $c^+a_1-c^-a_2$  intersections, there are sharp depolarization areas that burst perpendicularly into the main domain wall (highlighted with arrows in Figure 2a-c). That is, the effective domain wall width increases significantly in these areas. Secondly, also without these bursting areas of depolarization, the domain wall in the middle of a bundle domain (*B*) is much thinner (50%) than the ferroelectric domain wall that coincides with the multiple twinning planes of the bundle wall itself (*A*). As presented in Figure 2e, by fitting to a Lorentzian the 29 averaged sequential cross-section curves that go through the domain wall, a 12.5 nm domain wall width was measured (the cross-sections were taken from the area designated by a yellow line in Figure 2d). A hyperbolic tangent fit of the averaged phase cross-sections from the same area is shown for comparison in Figure 2f, demonstrating that a 0.5 nm jump in phase is limited by the pixel resolution of the scan. Since the depolarization area in wall *A* is rather disordered, averaging a large number of sequential cross-sections was impractical. Hence, a typical ca. 25 nm width domain wall was evaluated from multiple cross-sections that were taken from areas that were chosen arbitrarily. We should note that to avoid experimental artefacts (e.g., due to domain tilting), both the forward and backward scans were considered (Figure S12). Moreover, the laser-cantilever-photodiode axis was aligned prior to the imaging to avoid cross-talk between the out-of-plane and in-plane piezoresponse signals. Furthermore, the appearance of the striped ferroelastic domains in the topography image strongly supports our domain analysis.

In addition to the two-dimensional twinning defects, we observed also an extended structural defects that mediates the different types of the two-dimensional defects. Highlighted in the dashed yellow frame in Figures 2b-c, a split stripe domain was located very close to the cornered meeting point between boundaries *A* and *B* (and *C*). Such a split indicates on the existence of a needle domain that allows a rapid deformation of the material structure, being the meeting point of *a* and *c*

domains.<sup>[28]</sup> In fact, it is impossible determine whether split domains as the one that is currently discussed are indeed needle domains, or whether they are dislocations such as, edge, screw or any other similar deformation (although the first is the most plausible). However, in either case, this local structural defect has a corresponding Burgers vector that is perpendicular to the split stripes (as exemplified in Figure S13). This defect adds a slip plane and divides the ferroelectric domains almost symmetrically through the cornered meeting point of boundaries *A* and *B*.

#### 4. Discussion and Conclusions – Topological Analysis

Landauer emphasized that the energy associated with a domain wall is proportional to its surface area.<sup>[28]</sup> Hence the observed increase in domain wall surface area as a result of increase in defect concentration suggests that ferroelectric domain walls use lattice defects for stabilization. In fact, summarizing the observations, one can conclude that the mesoscopic ferroelectric domain wall is pinned by a complex network of crystallographic defects that is composed of three different mechanisms: (i) plane defects: a long bundle domain wall with high-concentration of ordered twinning planes of alternating directions and wedged ferroelastic domains (boundary *A*); (ii) plane defects: a long wall with distorted stripes that locally look like a bundle domain boundary (boundary *B*), but as opposed to a true bundle domain boundary (boundary *A*) the transition between  $c^+$  and  $c^-$  domains does not have to be directly through an *a* domain; and (iii) a local extended structural defect (split domain) that exerts sheer strain in the center of the domain and mediates between the other two boundaries. This complex network of crystallographic defects is reminiscence of the Frank-Read mechanism in materials.<sup>[29]</sup>

In ferroics, the domain wall width is determined by two competing mechanisms. For instance, in ferromagnetism, the first is the strength of the interaction between the spins (*J*), while the second is the magnetocrystalline asymmetry. Clearly, there is no reason for *J* (which now represents the dipole-dipole interaction) to change across the PZT film. This means that the observed difference in domain-wall width between boundary *A* and boundary *B* is due to differences in the local symmetry. Hence, we wanted to clarify the origin of this local change in symmetry.

A formula for domain wall widths  $\delta$ , in terms of the film thickness *d* and the domain spacing (domain width) *w* was suggested by Catalan *et al.*<sup>[30]</sup>

$$\delta = w^2 / dG \quad (1)$$

where  $G = 1.765(\epsilon_{\perp}/\epsilon_{\parallel})^{1/2}$  is a dimensionless constant whereas  $\epsilon_{\perp}$  ( $\epsilon_{\parallel}$ ) is the perpendicular (parallel) dielectric constant. The 1.765 arrives from the Riemann function of argument 3. Equation (1) is valid when periodic domains are in mechanical equilibrium, while we expanded its framework to examine the stability of bundle domains. Therefore, if the domain wall thickness suddenly changes from 25 nm to 12.5 nm for a given domain (*i.e.*, without an increase in domain width *w* by a factor

of 141%), it may imply that the meeting-point between A and B (where we observed the split domain) is not in mechanical equilibrium. Therefore, we can conclude that in this case, the mediating effect of the extended structural defect (split domain) is only metastable and not in equilibrium.

In addition to the difference in the domain wall, we can follow the analysis of domain stabilization with twinning defects following the derivation of Bornarel *et al.*, who suggested three mechanisms for domain stabilization at temperatures much lower than the Curie temperature<sup>[2]</sup> (for PZT  $T_c \gg 300$  K). The first mechanism is associated with regions (or whole specimens) of very high crystal quality, where the probability of a domain wall to introduce additional twinning planes is very low. This is because here, the creation energy of a twinning defect is much higher than the energy required for introducing a local structural defect or for gliding the defect. This mechanism may explain boundary B. The second mechanism is valid for 'medium quality crystals' or regions in ceramics. Here, the twinning-dislocation creation energy is lower than the gliding energy. This scenario describes boundary A, which is occupied by a large number of twinning dislocations and a broad and disordered depolarized ferroelectric domain wall. The last relevant mechanism suggests that when the twinning creation energy and the gliding energy are comparable, the domains glide parallel to the twinning plane, giving rise to a lateral displacement of the domain wall. Such a lateral collapse was indeed observed in the extended structural defect that is a result of the split domain. That is, this deformation allows a domain intersection that mediates energetically between the domain wall A, in which the formation of twinning planes at the polarization domain wall is energetically favorable, and domain wall B, which does not have such twinning planes. This leads us to a notable conclusion that although split domains are localized vertices (they are more localized than the plane defects in the case of twinning), they stabilize the walls of large mesoscopic or macroscopic domain. An equivalent statement would be that extended structural defect pin ferroelectric and ferroelastic domains.

We should note that in magnets, the lateral collapse of domain walls is well known. In particular, the Walker breakdown is a manifestation of such collapse. However, such phenomena are generally due to high domain wall velocities and unreported in ferroelectrics. As Yan *et al.* remark,<sup>[31]</sup> 'In flat strips, the Walker breakdown of a transverse wall is initiated by the nucleation of a vortex (or anti-vortex), which always enters from the lateral boundary.' As discussed above, the presence of a structural defect as a result of a split domain may greatly influence such lateral domain wall collapse in ferroelectric domains, while the analogy with Walker breakdown should be explored further. We would like to note that it has already been demonstrated that artificial extended structural defects that are reminiscent of the structure of a split domain can give rise to vorticity of electrons.<sup>[32]</sup>

Bornarel *et al.* discussed the energy profile of these mechanisms by means of interacting vertices,<sup>[2]</sup> which represent the extended structural defects (not to be confused with vortex domains). The vertex-vertex interaction was quantified by Srolovitz and Scott<sup>[33]</sup> in terms of a vector-Potts model. In the vector-Potts model (also called the four-state clock model), the interaction part of the Hamiltonian is given by:

$$H^{\text{Potts}} = -J \sum (\theta_i - \theta_j) \quad (2)$$

where  $\theta_i = 2\pi s_i/Q$  is the vector spin;  $s_i$  is the spin state (the summation is of all  $i$ 's and  $j$ 's); and  $Q$  represents the degeneracy of the system. The vector-Potts model suggests that both three-fold and four-fold vertices can be energetically stable as there is no change in energy, for instance, when the two boundaries separating  $\theta = 0$ ,  $\theta = \pi/2$  and  $\theta = \pi$  are degenerated to only one boundary, if the middle boundary ( $\theta = \pi/2$ ) is removed. Moreover, Srolovitz and Scott demonstrated that a four-fold vertex can be created by coalescing two vertices that are three-fold. Recently, these have been studied in detail by McQuaid,<sup>[34]</sup> while we also reported of interacting vertices of higher orders of symmetry.<sup>[29]</sup> Hence, the domain wall discussed in the current paper supplies a 'frozen' image of a complete topological path. That is, the locally distorted domains in wall B comprise a high concentration of uncorrelated threefold vertices (Figure 3a). Then, the split domain (*i.e.* an extended structural defect) that is embedded exactly at the meeting point between areas A and B and that is ending at a bundle domain, binds together two threefold vertices (Figure 3b). Such threefold vertex pairs in close proximity, connected by short domain walls, have interesting head-on collisions.<sup>[34]</sup> Moving further along the domain wall towards area A, the vertices represent multiple twinning walls of the  $c^+a_1c^-a_2$  bundle domain boundary, *i.e.*, fourfold

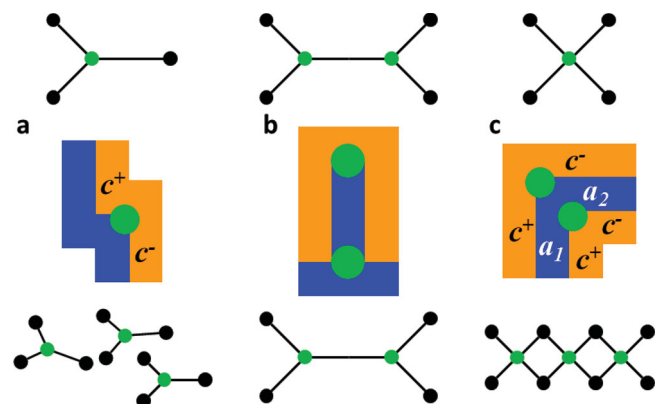


**Figure 3.** Micro and meso scale topological phase transition in ferroelectrics. (a) Threefold vertices (top) are formed by distorted stripe domains (middle) and are locally correlated on a mesoscopic scale (bottom). This represents the areas in Figure 2b that are highlighted by arrows at boundary B and, in which the striped domains are distorted, as appear clearly in Figure 2d (and in Figures S11f-h). (b) At the end of the mesoscopically-correlated vertices, two adjacent threefold vertices interact (top), *e.g.*, by a structural defect as a result of a split domain (middle), giving rise to a change in the mesoscopic symmetry of the system (bottom). The structure of such split domain is highlighted by a yellow square in Figure 2b and in the corresponding schematics in Figure 2c (and in Figures S11c-d). (c) On the other side of the edge of the split domain, there is an ordered phase in which the two interacting threefold vertices are coalesced into a fourfold vertex (top), *e.g.*, by the formation of a bundle domain boundary with  $a_1$ - $c$ - $a_2$  intersections (green points in the middle schematics). Moreover, the existence of multiple adjacent  $a_1$ - $c$ - $a_2$  intersections, essentially forms a network of four-point vertices (bottom). Such a bundle domain boundary with organized periodic vertices corresponds to the depolarized  $a_1$ - $c$ - $a_2$  intersections at boundary A as seen in the micrograph in Figure 2b as well as in the schematics in Figure 2c (and in Figures S11c-e).

vertices (Figure 3c). Therefore, the domain walls in Figures 1 and 2 demonstrate that a mesoscopic ferroelectric domain wall can be pinned by the topological path of interacting vertices, formed by different types of extended structural defects, in agreement with the predictions of both Bornarel *et al.* and of Srolovitz and Scott. Moreover, the studied domain distribution demonstrates that such a topological path is stabilized with the structural defect associated with a split domain.

In addition to the electro-mechanical (or electro-elastic) interactions at the atomic scale, this topological path can accurately describe the mesoscopic structure of the system. That is, moving from wall *B* to wall *A* through the structural defect as a result of the split domain, the mesoscopic organization of the system follows the nanoscale symmetry. Hence, such a topological path signifies the role of ferroelasticity and extended structural defects in the scalability of ferroelectricity.

## 5. Direct Observation of Pinning Dynamics

In addition to the above study of static domains, a dynamic examination of the pinning process can significantly support the discussed analysis. Such a dynamic study is accomplished by investigating the out-of-plane polarization evolution under external excitation as a function of extended structural defects such as those associated with split domains. In practice, we compared domain switching in the absence of a split domain with domain switching in the presence of a split domain. The experimental scheme involved imaging first the native twinning and out-of-plane polarization in an area. Then, we applied a DC electric field (higher than the coercive value) between the AFM tip and the bottom electrode upon which the PZT was deposited; and finally, we imaged the resultant domain distribution. Figure 4 demonstrates that in the absence of any apparent local structural defects (*i.e.*, split domains), local domain switching

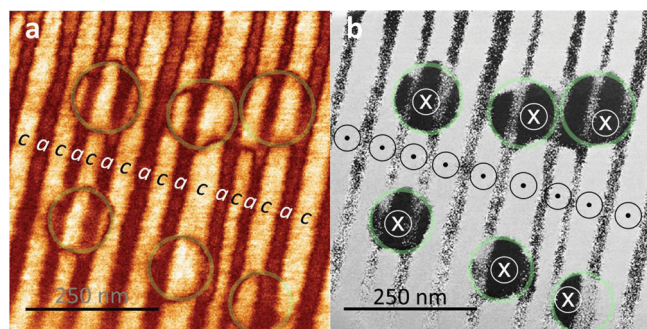


**Figure 4.** Local out-of-plane polarization reversal in a polywitin in the absence of extended structural defects in PZT. An area within a bundle domain after the polarization was reversed locally while applying 8 V between the AFM tip and the bottom Pt electrode (the coercive value is  $\sim 2$  V). (a) E-PFM amplitude image demonstrates that the periodic striped ferroelastic *a-c* twinned domains are not distorted. (b) E-PFM phase image of the same area reveals the mesoscopic ferroelectric domain distribution in the area (*i.e.*, the out-of-plane polarization domains that may include several *a* and *c* domains, as explained elsewhere.<sup>[34]</sup> The approximated rounded ferroelectric domain walls are highlighted, with radii (in nm, clockwise from top left): 64, 63.5, 68.5, 57, 59 and 58.5. Data reproduced with permission.<sup>[35]</sup> © 2010 American Physical Society.

(at six different sites) gave rise to homogeneous out-of-plane domains with circular symmetry. That is, no apparent structural defects were created, so that the out-of-plane mesoscopic polarization domains assume a uniform shape.<sup>[35]</sup>

Bearing in mind Landauer's framework, the domain size is dictated by an energy balance associated with the domain creation:

$$G = -U_{\text{tip}} + U_{\text{wall}} + U_{\text{depolarization}} \quad (3)$$

where  $U_{\text{tip}} = EP_s v$  and  $U_{\text{depolarization}} = 4 \cdot (P_s^2 / \epsilon_0 \epsilon_r) \cdot v$  are proportional to the domain volume ( $v$ ). Assuming that the circular surface corresponds to cylindrical domain:  $v = S \cdot t$ , and  $U_{\text{wall}} = \sigma \cdot L \cdot t$  is proportional to the domain wall area  $L \cdot t$ . Here,  $E$  is the applied field (we used the plate capacitor approximation:  $E = V/t$ ),  $\sigma$  is the domain wall energy per unit area,  $P_s$  is the spontaneous polarization,  $\epsilon_0$  and  $\epsilon_r$  are the dielectric constant of the vacuum and of the film,  $S$  is the area of the circular top surface of the domain and  $L = 2 \cdot (\pi \cdot S)^{1/2}$  is the perimeter of this area. It is interesting to note that the circular symmetric shape of the domain is preserved despite the fact that the out-of-plane polarization domain (mesoscopic ferroelectric domain) spans several ferroelastic (*a-c*) twinned domains, *i.e.*, there are periodic regions with in-plane polarization within the switched out-of-plane circular polarization domain (*a* domains in Figure 4).

To examine the influence of extended structural defects on ferroelectric domains (*i.e.*, pinning), we repeated the experiment in an area in the sample that contained a split domain in the native domain distribution as shown in Figure 5. Similarly to the previous case, an out-of-plane polarized domain that spans several ferroelastic domains was formed. However, the shape of the switched domain was distorted. That is, the split domain clearly pinned part of the domain wall, preventing it from spreading isotropically (*i.e.*, the formed domain had an incomplete circular surface). Thus, not only does this demonstrate directly the pinning process of a ferroelectric domain by a split domain, but it also exemplifies the influence of such defects on domain faceting.

## 6. Energy Estimation of Pinned and Distorted Domains

We propose a method to calculate the energy associated with ferroelectric domain distortion, *e.g.*, as a result of pinning. Although this method can be generalized also to pinning due to other factor and even to other general mechanisms that disturb the domain geometry, we exemplify it for the case of local extended structural defects (split domains). Specifically, Equation (3) allows a direct calculation of the domain energy as a function of film thickness, domain perimeter and domain volume when  $V$ ,  $\sigma$  and  $P_s$  are known (we used:  $\epsilon_r = 1700$ ).<sup>[36]</sup> Using the Sawyer-Tower method (where we used a 1 mm diameter top Pt electrode in parallel to a 198 nF capacitor) we measured  $P_s = 18.4 \pm 0.4 \mu\text{C cm}^{-2}$ . Moreover, the requirement of minimum energy in the unperturbed case in Figure 4 ( $\langle r \rangle = 61.8$  nm) allowed us to extract the domain wall energy of our PZT films from the derivative of Equation (3) with respect to  $r$ :

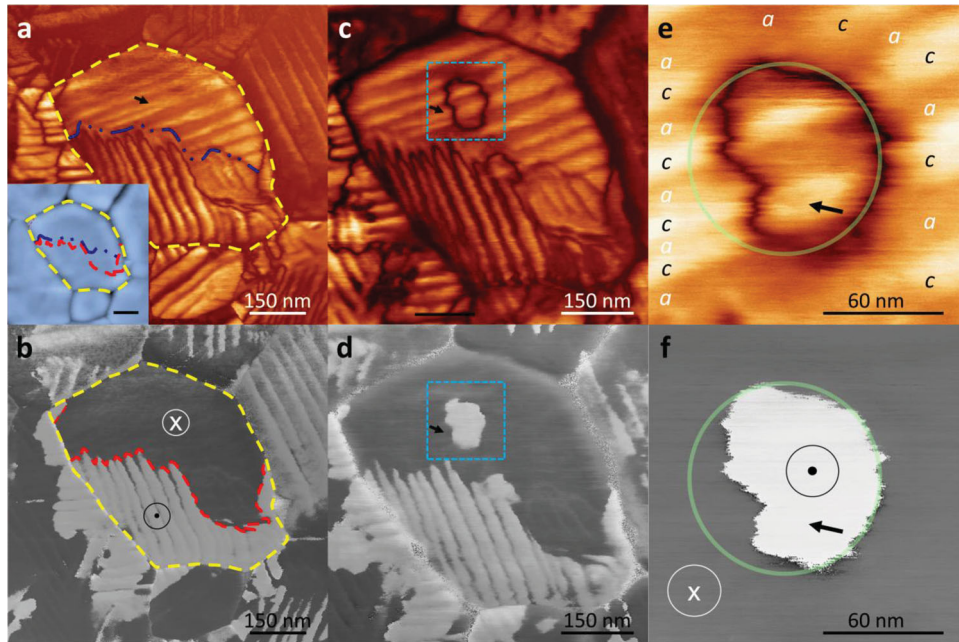


**Figure 5.** Local polarization reversal in the presence of extended structural defects. (a) E-PFM amplitude image of the native ferroelastic domain distribution (stripes) in a large grain (insert: topography) with a split domain (highlighted). (b) Bright and dark regions in the phase image correspond to up and down out-of-plane polarization in the same area (twinned domains are also distinguishable, but with lower contrast). Dashed lines (blue, red and yellow) help guide the eye for bundle domain-, mesoscopic ferroelectric domain- and grain- boundaries, while ferroelectric-domain walls also appear as dark lines in the amplitude imaging. (c) Applying 8 V (DC) between the stationary AFM tip and the bottom electrode at the middle of a bundle domain (at the center of the marked region) did not change the ferroelastic domain distribution (striped domains). However, (d) the external field switched locally the out-of-plane polarization. The split domain (marked with in-plane arrows) pinned the ferroelectric domain, destroying the circular symmetry of the switched domain. (e-f) are smaller area scans ( $160 \times 160 \text{ nm}^2$ , marked in (c-d)) around the switched domain, highlighting the asymmetric polarization domain shape (f) due to the domain pinning as a result of the local structural defect (split domain) (e). The  $a$ - $c$  domain and the out-of-plane domain distributions are marked in (e) and (f). The area of the switched domain is  $S = 5700 \text{ nm}^2$  and the domain wall length is  $290 \text{ nm}$ , while the radius of the circular extrapolation (transparent green circles) is  $r = 47.6 \text{ nm}$ .

$$\sigma = rP_s(E - 4P_s / \epsilon_0 \epsilon_r) \quad (4)$$

Here,  $\sigma = 0.96 \text{ J m}^{-1}$ . Hence, given that  $t = 60 \text{ nm}$ , we measured  $L$  and  $S$  directly from Figures 4 and 5. Therefore, we could compare the energies of the unperturbed domains in Figure 4:  $G_{\text{unperturbed}} = G(r = 68.4 \text{ nm}) = 1.18 \cdot 10^{-14} \text{ J}$  with the domain that was pinned by a split domain as shown in Figure 5 ( $L = 290 \text{ nm}$  and  $S = 5700 \text{ nm}^2$ ):  $G_{\text{pinned}} = 1.15 \cdot 10^{-14} \text{ J}$ .

We assumed that in all cases, the film parameters in Equation (3) are identical, and the only change is the mesoscopic domain geometry. Therefore, we can directly evaluate the pinning energy:  $\Delta G_{\text{pinning}} = G_{\text{pinned}} - G_{\text{unperturbed}} = 3 \cdot 10^{-16} \text{ J}$ . In practice, this 3% difference is within the experimental error, suggesting that although pinning due to split domains distorts the ferroelectric domain geometry, the energy stored in the unperturbed domains in Figure 4 is similar to the energy stored in the pinned domain in Figure 5.

An alternative approach to study the pinned domains suggests that although the macro scale and mesoscale film parameters are almost identical in Figure 4 and 5, the nanoscale parameters might not necessarily be so. For instance, we assumed a homogeneous mesoscopic domain, while there might be an influence of the small change in the  $a$ - $c$  domain

periodicity. Moreover, the intrinsic  $P_s$  value might be slightly different. Bearing into account these parameters is straight forward and in fact, it is not expected to change the relative comparisons between the energy of the different domains. Yet, for the sake of accuracy, one may seek for a different reference for the unperturbed domain. An upper limit for such a reference is obtained by extrapolating the pinned domain to a cylinder. That is, we compare the pinned domain, which is distorted, to a perfect cylindrical domain that is an extrapolation of this distorted domain, in contrast to the previous comparison that we made to a different domain with a 'true' circular symmetry. Specifically, we assume that the extrapolated circular structure represents the unperturbed domain (light green circle marks in Figures 5e-f), so that its energy can be compared to that of the pinned domain (the actual imaged domain wall in Figures 5e-f). Here, substituting  $r = 47.6 \text{ nm}$  in Equation (4) gives rise to  $\sigma = 0.74 \text{ J m}^{-1}$ . Consequently, the energy of the extrapolated unperturbed domain is:  $G_{\text{unperturbed}}^* = 6.6 \cdot 10^{-15} \text{ J}$  (which is about half of  $G_{\text{unperturbed}}$  that was extrapolated from Figure 4). This is in comparison to the energy of the pinned domain in Figure 5 ( $S = 5700 \text{ nm}^2$  and  $L = 290 \text{ nm}$ ):  $G_{\text{pinned}} = 7.65 \cdot 10^{-15} \text{ J}$ . Thus, an upper limit for the pinning energy is:  $\Delta G_{\text{pinning}} = G_{\text{pinned}} - G_{\text{unperturbed}}^* = 1.0 \cdot 10^{-15} \text{ J}$ , which corresponds to a 15% difference in energy due to the domain pinning.

## 7. Summary

To conclude, we discussed in detail the role of extended structural defects in stabilizing and pinning ferroelectric domain walls. In particular, we explained the interplay between extended structural defects and domain wall energy. Moreover, we demonstrated the coexistence of the three possible domain walls proposed by Bornarel *et al.*, explaining how it allows a complete topological path, which in turn gives rise to mesoscopic scalability of the ferroic systems. Lastly, we suggested a method to study the energy associated with domain wall pinning through a direct observation of the domain dynamics and we implemented this method to study the pinning energy due to a split ferroelastic domains.

## 8. Experimental Section

Imaging was carried out using an Asylum MFP-3D, with Pt/Cr coated ContE cantilevers from Budget-Sensors, resonant frequency: 11–14 kHz, nominal force constant: 0.2 N m<sup>-1</sup>. Details about the E-PFM method can be found elsewhere.<sup>[26,35–38]</sup> The images were analyzed with WsXM.<sup>[37]</sup>

## Supporting Information

Supporting Information is available from the Wiley Online Library or from the author.

Received: December 23, 2013

Revised: April 27, 2014

Published online:

- [1] J. C. Toledano, J. Schneck, *Solid State Commun.* **1975**, *16*, 1101.  
 [2] J. Bornarel, J. Lajzerowicz, J. F. Legrand, *Ferroelectrics* **1974**, *7*, 313.  
 [3] J. F. Scott, *Science* **2007**, *315*, 954.  
 [4] C. Lenser, Z. Connell, A. Kovács, R. Dunin-Borkowski, A. Köhl, R. Waser, R. Dittmann, *Appl. Phys. Lett.* **2013**, *102*, 183504.  
 [5] K. Aizu, *J. Phys. Soc. Japan* **1969**, *27*, 387.  
 [6] E. K. H. Salje, *Annu. Rev. Mater. Res.* **2012**, *42*, 265.  
 [7] W. Jo, J. E. Daniels, J. L. Jones, X. Tan, P. A. Thomas, D. Damjanovic, J. Rödel, *J. Appl. Phys.* **2011**, *109*, 014110.  
 [8] Y. Ivry, J. F. Scott, E. K. H. Salje, C. Durkan, *Phys. Rev. B* **2012**, *86*, 205428.  
 [9] Y. Ivry, D. P. Chu, C. Durkan, *Nanotechnology* **2010**, *21*, 065702.  
 [10] A. Garcia-Melendrez, C. Durkan, *Appl. Phys. Lett.* **2013**, *103*, 092904.  
 [11] D. M. Evans, A. Schilling, A. Kumar, D. Sanchez, N. Ortega, M. Arredondo, R. S. Katiyar, J. M. Gregg, J. F. Scott, *Nat. Commun.* **2013**, *4*, 1534.  
 [12] E. Simon, F. Borodavka, I. Gregora, D. Nuzhnyy, S. Kamba, J. Hlinka, A. Bartaszyte, S. Margueron, *J. Appl. Phys.* **2011**, *110*, 084115.  
 [13] V. Janovec, J. Pívratská, presented at *Int. Meeting Ferroelectrics* Krakow, Poland, September **2013**.  
 [14] L.-W. Chang, V. Nagarajan, J. F. Scott, J. M. Gregg, *Nano Lett.* **2013**, *13*, 2553.  
 [15] R. Ahluwalia, N. Ng, A. Schilling, R. G. P. McQuaid, D. M. Evans, J. M. Gregg, D. J. Srolovitz, J. F. Scott, *Phys. Rev. Lett.* **2013**, *111*, 165702.  
 [16] A. Kumar, R. S. Katiyar, J. F. Scott, *Nanoscale* **2014**, *6*, 1064.  
 [17] A. Schilling, S. Prosandeev, R. G. P. McQuaid, L. Bellaiche, J. F. Scott, J. M. Gregg, *Phys. Rev. B* **2011**, *84*, 064110.  
 [18] I. Vrejoiu, G. Le Rhun, N. D. Zakharov, D. Hesse, L. Pintilie, M. Alexe, *Philos. Mag.* **2006**, *86*, 4477.  
 [19] T. Tybell, P. Paruch, T. Giamarchi, J.-M. Triscone, *Phys. Rev. Lett.* **2002**, *89*, 097601.  
 [20] Y. W. So, D. J. Kim, T. W. Noh, J.-G. Yoon, T. K. Song, *J. Korean Phys. Soc.* **2005**, *46*, 40.  
 [21] S. M. Yang, J. Y. Jo, D. J. Kim, H. Sung, T. W. Noh, H. N. Lee, J.-G. Yoon, T. K. Song, *Appl. Phys. Lett.* **2008**, *92*, 252901.  
 [22] P. Paruch, J. Guyonnet, *Comptes Rendus Phys.* **2013**, *1*, 1.  
 [23] Y. Ivry, D. Chu, J. F. Scott, C. Durkan, *Adv. Funct. Mater.* **2011**, *21*, 1827.  
 [24] A. Gruverman, *J. Vac. Sci. Technol. B Microelectron. Nanom. Struct.* **1995**, *13*, 1095.  
 [25] N. Balke, I. Bdikin, S. V. Kalinin, A. L. Kholkin, *J. Am. Ceram. Soc.* **2009**, *92*, 1629.  
 [26] Y. Ivry, D. Chu, C. Durkan, *Appl. Phys. Lett.* **2009**, *94*, 162903.  
 [27] Y. Ivry, D. P. Chu, J. F. Scott, C. Durkan, *Phys. Rev. Lett.* **2010**, *104*, 207602.  
 [28] E. K. H. Salje, Y. Ishibashi, *J. Phys.: Condens. Matter.* **1996**, *8*, 8477.  
 [29] R. Landauer, *J. Appl. Phys.* **1957**, *28*, 227.  
 [30] Y. Ivry, D. P. Chu, J. F. Scott, E. K. H. Salje, C. Durkan, *Nano Lett.* **2011**, *11*, 4619.  
 [31] G. Catalan, J. F. Scott, A. Schilling, J. M. Gregg, *J. Phys. Condens. Matter* **2007**, *19*, 022201.  
 [32] M. Yan, C. Andreas, A. Kákay, F. García-Sánchez, R. Hertel, *Appl. Phys. Lett.* **2011**, *99*, 122505.  
 [33] J. Verbeeck, H. Tian, P. Schattschneider, *Nature* **2010**, *467*, 301.  
 [34] D. Srolovitz, J. Scott, *Phys. Rev. B* **1986**, *34*, 1815.  
 [35] R. McQuaid, *Ph.D. Thesis*, Queens University of Belfast, **2012**.  
 [36] Y. Ivry, N. Wang, D. Chu, C. Durkan, *Phys. Rev. B* **2010**, *81*, 174118.  
 [37] T. S. Low, W. Guo, *J. Microelectromechanical Syst.* **1995**, *4*, 230.  
 [38] I. Horcas, R. Fernández, J. M. Gómez-Rodríguez, J. Colchero, J. Gómez-Herrero, A. M. Baro, *Rev. Sci. Instrum.* **2007**, *78*, 013705.